ORIGINAL PAPER

Enn Lust · Gunnar Nurk · Silvar Kallip · Indrek Kivi
Priit Möller

Electrochemical characteristics of $Ce_{0.8}Gd_{0.2}O_{1.9}|La_{0.6}Sr_{0.4}CoO_{3-\delta}$ + $Ce_{0.8}Gd_{0.2}O_{1.9}$ half-cell

Abstract The analysis of the medium temperature half-cell $Ce_{0.8}Gd_{0.2}O_{1.9}$|70 wt% $La_{0.6}Sr_{0.4}CoO_{3-\delta}$ (LSCO) + 30 wt % $Ce_{0.8}Gd_{0.2}O_{1.9}$ (CGO) has been made by electrochemical impedance, cyclic voltammetry and chronoamperometry. The shape of complex impedance plots depends on temperature and cathodic polarisation of the electrode. Nyquist (Z'', Z'-) plots were fitted by equivalent circuit taking into account the electrolyte properties (at very high frequencies), charge transfer process at grain boundaries (at high frequencies), and medium and low frequency O_2 reduction process at the cathode surface and inside the porous cathode material. Two different time constants have been obtained for the cathode process, i.e. for electroreduction of oxygen. It was found that the addition of CGO into the cathode material (LSCO) only somewhat decreases the surface catalytic activity but the noticeably higher low-frequency resistance (i.e. mainly diffusion-like mass transfer resistance R_D) values at lower temperatures have been calculated. It was found that the mainly bulk diffusion-limited process at $T \leq 773$ K deviates toward the kinetically mixed process (diffusion + charge transfer) with increasing temperature.

Keywords Solid oxide fuel cell · $Ce_{0.8}Gd_{0.2}O_{1.9}$ · Mixed cathode · $La_{0.6}Sr_{0.4}CoO_{3-\delta}$ + $Ce_{0.8}Gd_{0.2}O_{1.9}$

E. Lust (✉) · G. Nurk · S. Kallip · I. Kivi · P. Möller
Institute of Physical Chemistry, University of Tartu,
2 Jakobi Street, 51013 Tartu, Estonia
E-mail: enn.lust@ut.ee
Fax: +37-27-375160

Introduction

Cobaltite perovskites are known to have very high catalytic activity toward oxygen reduction, high oxygen self-diffusion coefficients and high electrical conductivity values [1–14]. It should be noted that the high absorption or adsorption and faradaic charge transfer capacitancies, semi-infinite or finite length diffusion behaviour in the region of moderate ac frequency f [15–17], linear shape of cyclic voltammograms at moderate overpotential [18, 19] and strong correlation between electrode kinetics and bulk diffusion as well as surface exchange properties indicate the diffusion-like or mixed kinetic mechanism of the overall oxygen reduction reaction [20–26]. One possible method to increase the catalytic activity of the cathode is to enlarge the so-called three-phase boundary (TPB) length by adding the electrolyte powder (CGO) into the cathode material before fabrication of the cathodes on the solid electrolyte [27, 28]. Addition of the electrolyte into the cathode material has to decrease the thermal expansion coefficient of $La_{1-x}Sr_xCoO_{3-\delta}$(LSCO) and therefore to decrease the thermal compatibility problem of the LSCO cathode and electrolyte materials [15, 18, 26]. In designing of the cathodes for 500°C operation temperature an immediate problem arises because the diffusion process in the typical mixed conductors such as $La_{0.6}Sr_{0.4}Co_{1-y}Fe_yO_{3-\delta}$ (LSCFO) and $La_{1-x}Sr_xMnO_3$ (LSMO) has relatively high activation energies and bulk oxygen diffusion is reduced at lower temperatures [1, 12, 18, 20, 27, 28]. As $Ce_{0.9}Gd_{0.1}O_{1.95}$ and $Ce_{0.8}Gd_{0.2}O_{1.9}$ have higher oxygen diffusion rate in the solid phase than LSCFO at lower temperatures it becomes necessary to use composite cathodes [17, 18, 20, 25, 26]. As noted by Steele [22], as the volume fraction of CGO reaches the percolation threshold the cathode reaction series resistance is significantly reduced and will attain the target value of 0.2 Ωcm^2 for LSCFO + CGO|CGO interface at 600°C. It should be noted that high concentration of the vacancies and the mobility of lattice oxygen in the mixed conductors make it possible to extend the reaction zone from the TPB into the whole surface of the mixed conductor, whereas only the TPB is the reaction zone in a pure electronic conductor [15, 20, 22, 28]. It was found that the dominating contribution to the overall reaction (i.e. into the low frequency ac impedance) is described by two processes: (1) a Gerischer impedance in the fre-

quency range of around 1 Hz (so-called surface exchange process), (2) and a slower process described by a resistor in parallel to a constant phase element (R_{LF}/CPE_{LF}, i.e. to the faradaic charge transfer reaction, where the LF subscript stands for the very low frequency contribution) [15]. The total conductivity of LSCFO in air is predominantly p-type electronic and the total estimated apparent activation energy for the total conductivity is 12.2 ± 0.2 kJ mol^{-1} [27] or 13.5 kJ mol^{-1} [23].

It was found that the oxygen fluxes increase with decrease of thickness of $x\%$ La$_{0.8}$Sr$_{0.2}$Co$_{0.2}$Fe$_{0.8}$O$_{3-\delta}$ + (1-x)% Ce$_{0.8}$Gd$_{0.2}$O$_{1.9}$ membrane, but the specific oxygen permeability values are independent of thickness within the limits of experimental error. Such behaviour is in agreement with the integral form of Wagner law and unambiguously indicates that the oxygen transport is limited by the bulk ambipolar conductivity. Thus, the oxygen ionic transport in LSCFO + CGO composites might occur not only in the CGO phase, but also through the LSCFO phase [27]. X-ray diffraction (XRD) data for LSCFO|CGO and LSCFO + CGO|CGO composites confirmed the coexistence of two phases [27] with the perovskite and fluorite type structures, respectively. The expansion of CGO lattice is probably caused by incorporation of lanthanum and strontium cations, diffusing from LSCFO grains into the fluorite type (CGO) lattice [29]. Diffusion of gadolinium (or cerium) cations from CGO into the LSCFO phase is less probable because the thermodynamic stability of Gd-containing perovskites is lower than that of La-containing perovskite phases [30]. The smaller unit cell parameters of the perovskite phase in the composites with respect to pure LSCFO indicate a formation of A-site cation vacancies. Based on TEM data it was found that the interaction between LSCFO and CGO solid solution may result not only in the dissolution of lanthanum and strontium cations in the fluorite type lattice, but also formation of SrCeO$_3$-based isolating phases at the grain boundaries, not characterised by EDS method [27].

The oxygen exchange process from the gas phase into the Ce$_{0.8}$Gd$_{0.2}$O$_{1.9}$ electrolyte can be divided into a number of possible steps, including adsorption, dissociation and reduction of oxygen molecules (or atoms) and incorporation (absorption) of oxygen ions into the oxide bulk [1–20]. Each of these steps can determine the overall rate constant k^*/cm s^{-1} of oxygen surface exchange, i.e. can be a rate-limiting step. Manning et al. [31] suggested that the surface exchange process into the CGO could be simplified into two possible rate-limiting steps: a molecular dissociation step and the incorporation of oxygen into the CGO bulk. At $T \geq 700°C$ the dissociation of O$_2$ is a slow step in relation to the bulk incorporation (absorption) step. It was established that the oxygen exchange reaction on the CGO surface is limited by the availability of the electronic species for charge transfer. Therefore it seems that the concentration of free electrons limits the kinetics of the surface exchange process [32] and therefore the surface exchange

rate can be improved by adding the electronic conductor phase (for example Co$_3$O$_{4-\delta}$) into CGO or applying high cathodic polarisation [33].

The main aim of this work was to synthesise the 70 wt% LSCO + 30 wt% CGO cathode material and to obtain the electrochemical characteristics during long operation times, i.e. under the conditions of the repetitive thermocycling and long-lasting cathodic polarisation.

Experimental

Preparation of cathode materials and electrolytes

The LSCO powder was prepared by the conventional solid state reaction technique [20, 25, 34–37] from commercially available powders of La$_2$O$_3$ (99.99%), SrCO$_3$ (99.9%), Co$_3$O$_4$ (99.9%). Powders with the stoichiometric compositions were ball-milled in a zirconia mill container with zirconia grinding balls in H$_2$O for 3 h and after drying calcined at 1,473 K for 10 h to form a perovskite phase. The perovskite (trigonal R-3c at $T = 293$ K) phase was crushed and ball-milled for 3 h using the same ZrO$_2$ system. The XRD measurements indicate the formation of the single phase perovskite structure. The CGO electrolyte was prepared from the corresponding oxides CeO$_2$ (99.9%) and Gd$_2$O$_3$ (99.9%), using conventional solid-state reaction technique [14, 22]. Powders with the stoichiometric compositions were ball-milled for 3 h and calcined at 1,473 K in air for 10 h. The formed electrolyte material (cubic Fm-3m structure at $T = 293$ K, established by XRD method) was crushed and ball-milled in ethanol and, after adding an organic binder, were pressed into pellets with a diameter of 2 cm and thickness of 0.6 mm at the pressure $p = 20$ kN cm^{-2} for 0.5 min and sintered at 1,473 K for 10 h [35–37].

The mixed cathode material was prepared by mixing 70 wt% LSCO + 30 wt% CGO powders (synthesised and characterised before) with an appropriate amount of organic binder (ethyl cellulose) and solvent (turpentine oil), was screen-printed on one side of the CGO electrolyte as a working electrode with the surface area $S_{el} = 0.5$ cm^2. The working electrodes were fired at 1,323 K in air for 8 h and characterised by XRD and SEM methods before application of the counter and reference electrodes. A three-electrode assembly (Fig. 1) was used to study the electrochemical properties of the cathodes. The Pt counter and reference electrodes were prepared by screen-printing the Pt-paste (Engelhard) on the other side of the electrolyte, followed by sintering at 1,223 K for 2 h. The reference electrode (Pt|porous Pt|O$_2$) has been created into the hole prepared inside the solid electrolyte and the distance of the reference electrode to the working electrode was less than 10^{-2} cm. The lateral surface of the Pt-wire (i.e. the lateral surface of the reference electrode) has been isolated by quartz capillary tube, introduced into the electrolyte pellet
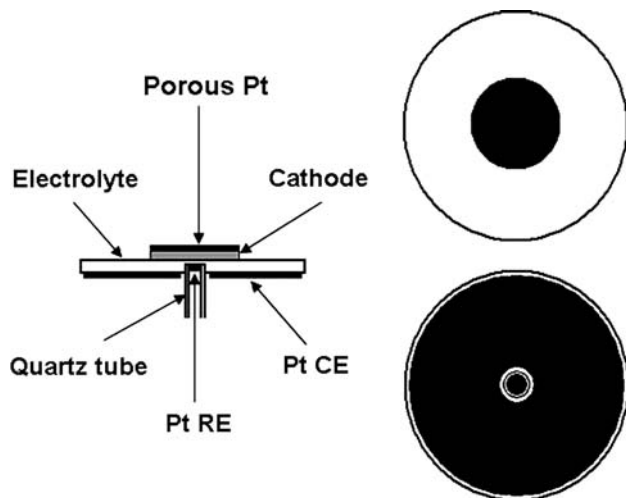
Fig. 1 Experimental setup used for semicell studies. Notation has been given in the figure

(Fig. 1). The areas of the Pt counter and Luggin-like reference electrodes were 3 cm^2 and 0.04 cm^2, respectively. The anode|electrolyte|cathode assembly was placed into the designed reactor and the cathode, reference electrode and anode were exposed to air. Three Pt wires were connected to the working, counter and reference electrodes and led to the cables of the potentiostat/galvanostat (type 1287, Solartron), frequency response analyser (type 1260, Solartron). The ac frequency f was changed from 10 MHz to 0.01 Hz. The ac voltage amplitude was 5 mV. The impedance spectra were recorded at ten points per decade. The ohmic series resistance R_{ex} of the system (bulk electrolyte + contact and Pt wire resistances) was determined from the impedance data at very high frequency $f \geq 5\times10^5$ Hz ($Z(\omega \rightarrow \infty) = R_{ex}$; $\omega = 2\pi f$) at $\Delta E = 0$ V (vs. Pt|porous Pt|O$_2$ reference electrode). The voltage range applied between the working and counter electrodes was not over 4 V for the extreme temperatures and polarisations ($\Delta E = -1.0$ V) used in this work.

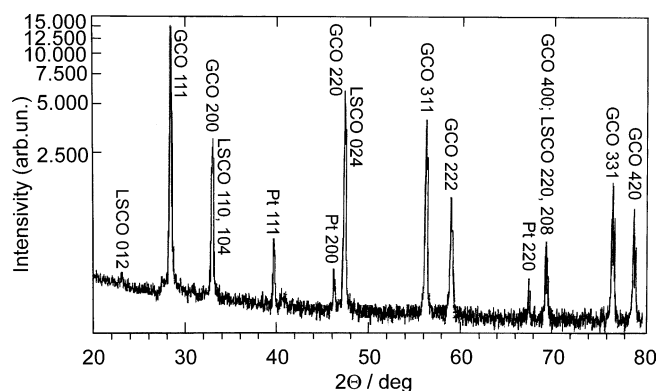The electrode materials have been characterised using XRD (Fig. 2), gas adsorption (BET) (Fig. 3) and AFM

(Fig. 4) methods. These cathode materials are porous with the specific surface area $S_{BET} \geq 20$ m^2 g^{-1} and there are transport pores ($d < 1\times10^{-6}$ m) as well as micro- and nano-pores with the mean diameter 1.8 nm (Fig. 3) inside the 70 wt% LSCO + 30 wt% CGO cathode material. Special big samples from 70%LSCO + 30%CGO, prepared under the same experimental conditions as the cathodes, have been used for the BET analysis. The size of particles varies from 0.5 μm to 2.5 μm, and the surface roughness factor R equal to 1.35 and the root mean square height of the cathode surface R_{ms} equal to 312 nm have been obtained from the AFM data (Fig. 4). The results of the electron microscopy studies demonstrate high porosity of the cathode, which is in a good agreement with STM and BET data.

Results and discussion

Experimental complex plane (Nyquist and Bode) plots

Figures 5a and 6a show the complex impedance plane (Z'', Z'-) plots for 70%LSCO + 30%CGO at different temperatures and electrode potentials ΔE (vs. Pt|porous Pt|O$_2$), where $Z'' = (j\omega\, C_s)^{-1}$ is the imaginary part and Z' is the real part of the complex impedance. For comparison, the Z'', Z'-data for La$_{0.6}$Sr$_{0.4}$CoO$_{3-\delta}$|CGO half-cell are given in Fig. 5b. The Z'', Z'-plots (Fig. 5a) display an inductive tail at

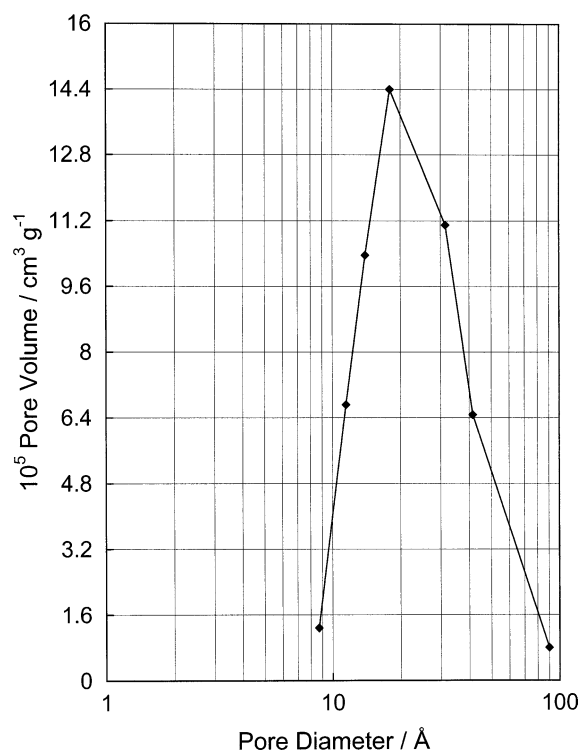Fig. 2 X-ray diffraction data for porous Pt|70 wt% La$_{0.6}$Sr$_{0.4}$CoO$_{3\,\delta}$ + 30 wt% Ce$_{0.8}$Gd$_{0.2}$O$_{1.9}$|Ce$_{0.8}$Gd$_{0.2}$O$_{1.9}$ interface, prepared according to explanations given in the text

Fig. 3 Incremental pore volume versus pore diameter plot for the 70 wt% La$_{0.6}$Sr$_{0.4}$CoO$_{3\,\delta}$ + 30 wt% Ce$_{0.8}$Gd$_{0.2}$O$_{1.9}$ cathode

Fig. 4 AFM images of microstructure, corresponding height profiles and the values of the root mean square height (R_{ms}) and surface roughness $R = S_{AFM}/S_{geom}$ for the 70 wt% $La_{0.6}Sr_{0.4}CoO_{3\,\delta}$ + 30 wt% $Ce_{0.8}Gd_{0.2}O_{1.9}$ cathode
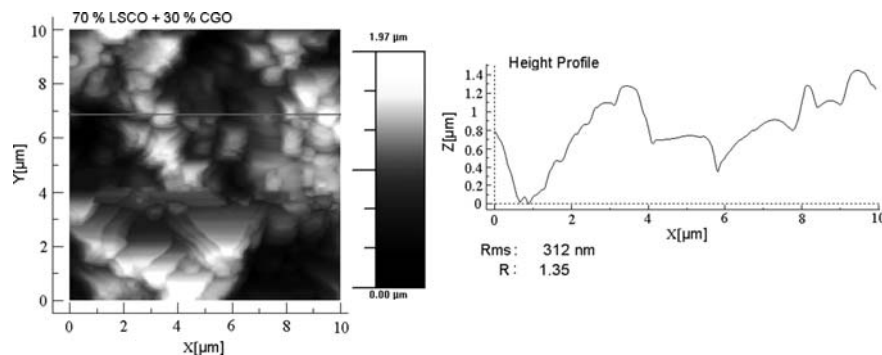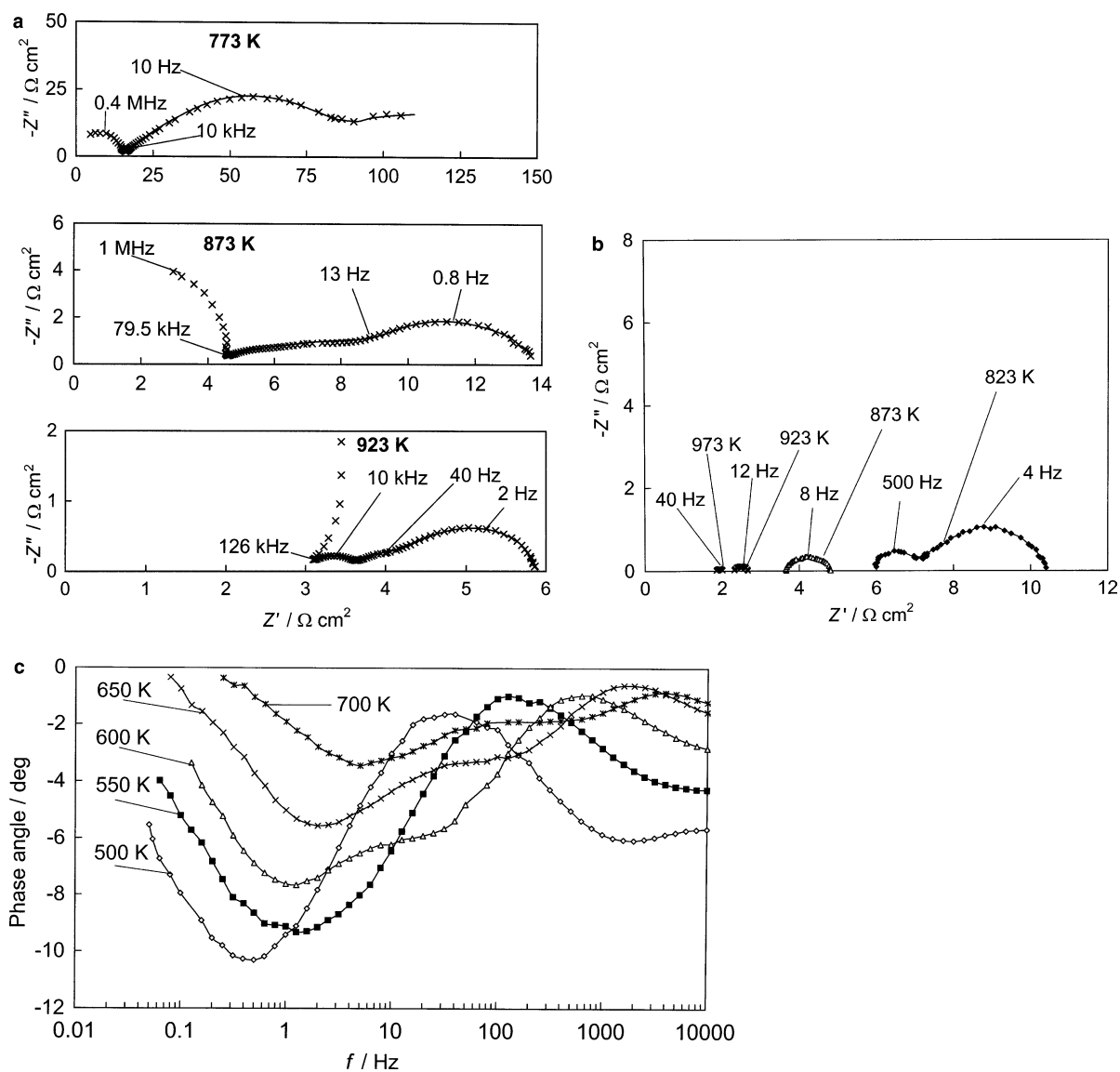

Fig. 5 Nyquist (Z'', Z'-) plots (at electrode polarisation $\Delta E = 0$) (**a**) and phase angle versus frequency plots at $\Delta E = -0.2$ V (**c**) for 70 wt% $La_{0.6}Sr_{0.4}CoO_{3\,\delta}$ + 30 wt% $Ce_{0.8}Gd_{0.2}O_{1.9}|Ce_{0.8}Gd_{0.2}O_{1.9}$ half-cell and Z'', Z'-plots for $La_{0.6}Sr_{0.4}CoO_{3\,\delta}|Ce_{0.8}Gd_{0.2}O_{1.9}$ interface at $\Delta E = -0.2$ V (**b**) at various temperatures T (K) noted in figure. (*Solid lines*: fitting according to circuit b in Fig. 7a)

very high frequencies $f > 4$ MHz and higher temperatures (not shown in figures) and a capacitive behaviour at frequency from 4 MHz to 0.01 Hz. The presence of the inductive tail at $f > 4$ MHz can be ascribed to the inductance of the measurement leads. In the region from 1 MHz to 5 kHz the two very well
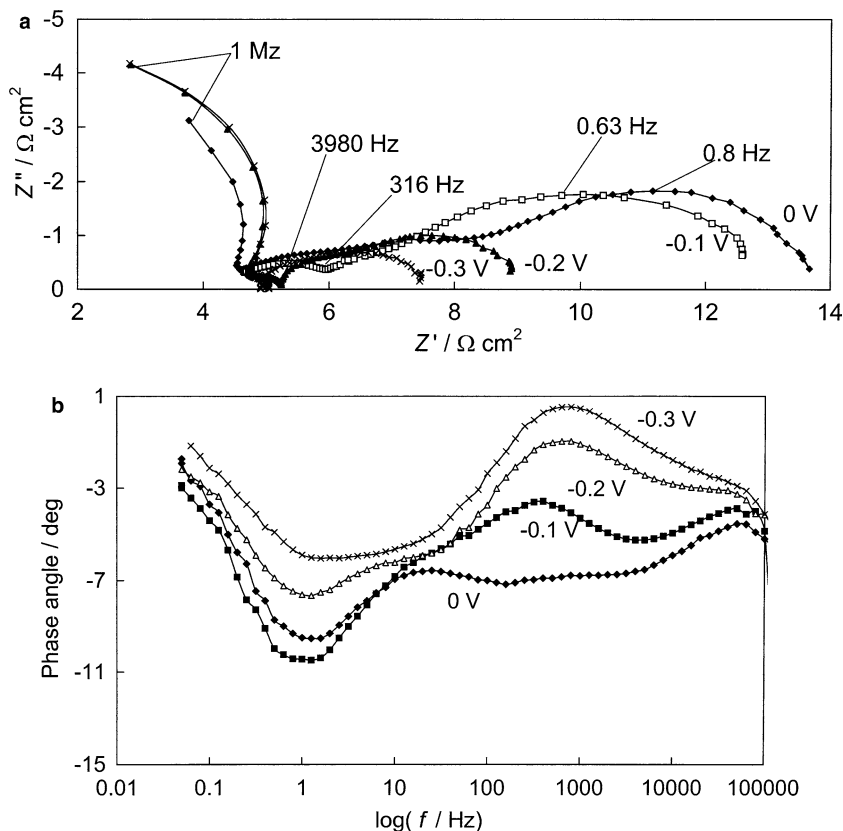
separable semicircles have been found, corresponding to the conductivity process in the bulk electrolyte (at $f > 100$ kHz) as well as to the O^{2-} ion transport at the cathode|electrolyte phase boundary (5 kHz $< f <$ 100 kHz). Usually the very high frequency semicircle is not fully developed, which is caused by very high relaxation frequency for the bulk conductivity process. These semi-circles do not correspond to the real electrochemical reduction processes [14, 17, 18, 35–37]. Comparison with the data for pure LSCO|CGO half-cell shows that the high-frequency part of the Z'', Z'-plots is mainly influenced by addition of CGO into LSCO i.e. by the more developed porous structure and TPB length, as for LSCO|CGO the high-frequency semicircles are very small compared with 70%LSCO + 30%CGO|system. In the region from 5 kHz to 0.01 Hz, at least two arcs (Fig. 5a), characterised by two time constants [$\tau = (2\pi f_{max})^{-1}$ where f_{max} is the frequency of the maximum in the Z'', Z'-plot], were observed at lower temperatures ($T < 873$ K). The medium-frequency arc (arc 1) is noticeably smaller than the low-frequency arc (arc 2). The shape of the medium-frequency arc 1 depends on T (i.e. the width of the arc1 corresponding to the polarisation resistance of the medium-frequency process, decreases with T), and the time constant τ_1 decreases with increasing T and describes the ionisation of adsorbed O_{ads} at the outer cathode surface with interfacial adsorption/absorption capacitance C_1. The width of the arc 1 depends on the cathode potential and the time con-

stant of the arc 1 decreases somewhat with the cathodic polarisation (Fig. 6a). The decrease in the phase angle $|\delta|$ with increasing temperature (Fig. 5c) at $T > 823$ K and with the rise of negative electrode potential (Fig. 6b) indicates that the "true" charge transfer process is the rate-determining step at $f > 10$ Hz ($\delta \approx -2°$ at $T \geq 873$ K and at $\Delta E \leq -0.2$ V). The so-called medium frequency arc 1 disappears with increasing T over 973 K.

The shape of the low-frequency arc 2 depends noticeably on T and ΔE (Figs. 5a, 6a), and this arc 2 becomes more depressed with increasing T and $|\Delta E|$, which can be explained by the less pronounced diffusion (i.e. mass transfer) limited behaviour at higher temperatures and negative potentials. The low-frequency arc 2 characterises the exchange reaction of oxygen from the gas phase into the nanopores of the porous cathode (i.e. electroreduction of O_{ads} to O_{ads}^-) and the slow diffusion of O_{ads}^- to the reaction zone inside the solid cathode material or at the surface of the nanopores. The time constant values for the arc 2 (τ_2) are independent of the electrolyte composition at fixed T and ΔE, and characterise mainly the properties and process in the 70%LSCO + 30%CGO system [35–37]. τ_2 noticeably decreases with the increase of T at fixed ΔE, and with the negative polarisation at fixed T. Comparison of the values of τ_1 and τ_2 for Sys1 with those for pure LSCO cathode [37] (Fig. 5b) shows that τ_1 and τ_2 and the so-called polarisation resistance increase with addition of CGO into the LSCO cathode material.
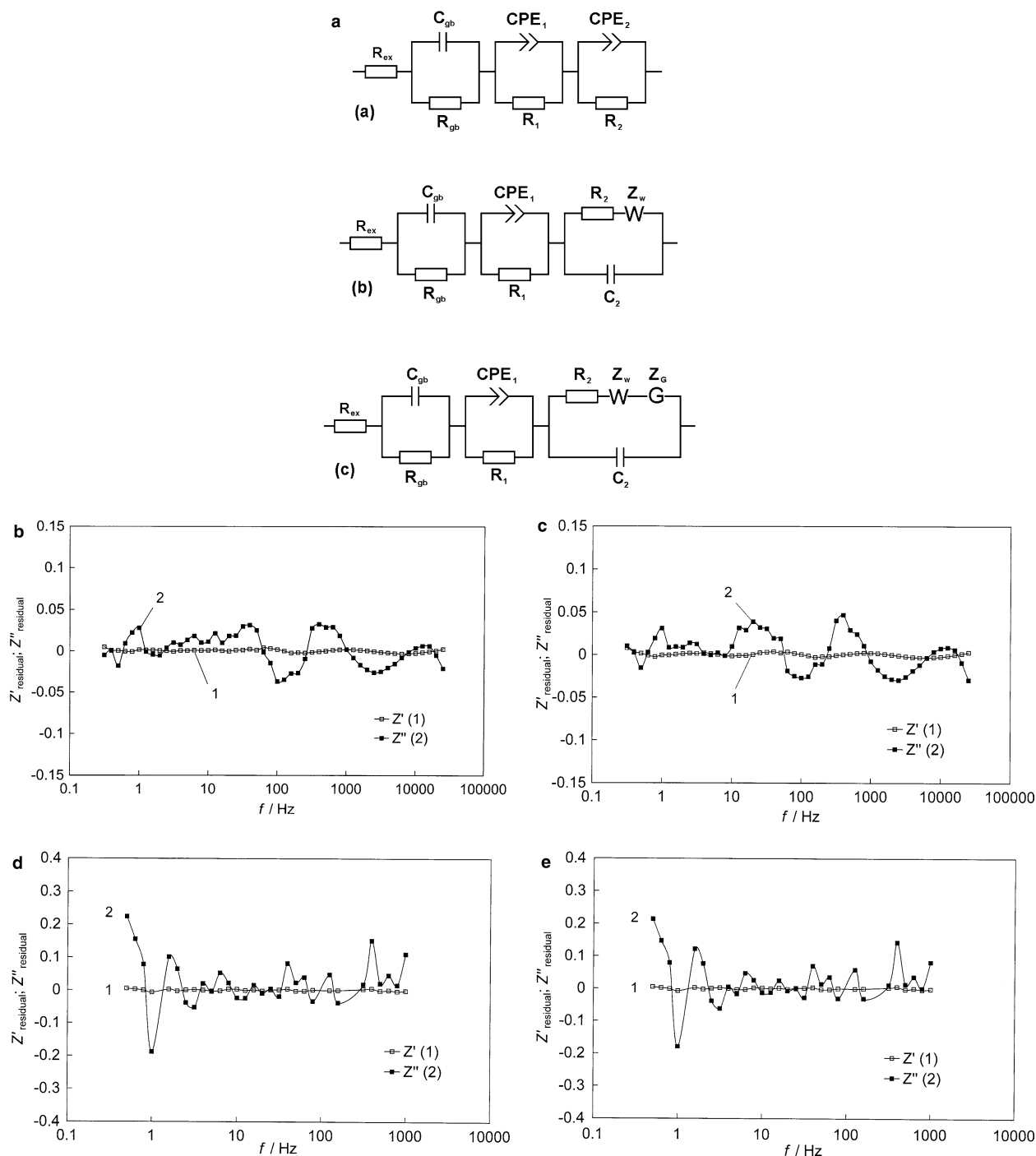
Fig. 7 a Equivalent circuits used for fitting the complex impedance plane plots. R_{ex} is the high-frequency series resistance ($R_{ex} \rightarrow Z'$ if $\omega \rightarrow \infty$); C_{gb} and R_{gb} are the grain boundary capacitance and resistance; CPE_1 and R_1 are the high-frequency constant phase element and resistance; CPE_2, R_2 and C_2 are the low-frequency constant phase element, resistance and capacitance; Z_W is the Warburg-like diffusion impedance; Z_G is Gerischer impedance. Relative residual Z''_{res}; Z'_{res}) versus frequency plots (**b–e**) for 70 wt% LSCO + 30 wt% CGO|CGO interface at $T = 773$ K and $\Delta E = -0.1$ V (**b, c**) and at $T = 873$ K and $\Delta E = -0.2$ V (**d, e**) in the case of circuit a (**c, e**) and circuit b (**b, d**) in Fig. 7a

Fitting of the Nyquist plots

The data in Figs.5a and 6a, to a first approximation, can be simulated by the equivalent circuit (solid lines–fitting, points–experimental), presented in Fig. 7a. For fitting the Z'', Z'-plots, the Zview 2.7 software has been used [38, 39]. The elements R_{gb} and C_{gb} in Fig. 7a characterise the grain boundary processes for the cathode|electrolyte phase boundary and, in comparison with

LSCO|CGO interface, the influence of R_{gb} and C_{gb} on the characteristics of the 70% LSCO + 30% CGO|CGO interface is very well detectable. It is mainly caused by the noticeably higher interface area between porous mixed cathode and electrolyte. The medium frequency as well as low frequency arcs can be fitted by the constant phase element CPE and charge transfer resistance connected in parallel (circuit a in Fig. 7a). The CPE impedance Z_{CPE} is equal to $A^{-1} (j\omega)^{-\alpha}$, where A is constant and α is the fractional exponent. If $\alpha = 1$, then A is equal to electrical double layer capacitance. The fractional exponent $\alpha_1 > 0.5$ and very low values of R_1 for the medium frequency arc 1 ($R_1 > 8$ Ωcm^2 at $T = 773$ K) indicate that the diffusion-like limited so-called "true" charge transfer process is the rate-determining step at $f > 10$ Hz and $T < 823$ K. (It should be noted that if $\alpha = 1.0$, $\alpha = 0.5$ and $\alpha = 0$, then CPE can be replaced by capacitor, infinite Warburg diffusional impedance and inverse charge transfer resistance, respectively, corresponding to the so-called capacitive, diffusion and charge transfer processes, respectively [38–42].) The fractal exponent values $\alpha_2 \approx 0.5$ for the low-frequency arc 2 indicate that CPE_2 behaves as a Warburg-type diffusional impedance Z_W. Thus, the CPE_2 can be exchanged to the generalised finite Warburg element (GFW) for a short circuit terminus model (circuit b in Fig. 7a) expressed as

$$Z_{GFW} = \frac{R_D \tanh\lfloor (jL2\omega/D)^{\alpha_w} \rfloor}{(jL^2\omega/D)^{\alpha_w}} \qquad (1)$$

where R_D is the limiting diffusion resistance, L is the effective diffusion layer thickness, D is the effective diffusion coefficient of a particle and α_w is a fractional exponent in Z_{GFW} [35–45]. If $\alpha_W = 0.5$ then the low-frequency process ($f < 10$ Hz) can be fitted by the classical Randles equivalent circuit [39–42]. The very small chi-square function values $\chi^2 < 2\times10^{-4}$ and weighted sum of squares $\Delta^2 < 0.020$ have been established, using the equivalent circuit b presented in Fig. 7a. The relative residuals Z'_{res} and Z''_{res} [38, 39] obtained are somewhat lower (especially Z'_{res} in the case of circuit b (Figs. 7b, d) compared with the circuit a (Figs. 7c, e), the residuals have random distribution and therefore the circuit b can be used for fitting the experimental Nyquist plots. The attempts to use the equivalent circuit c (given in Fig. 7a), where the Gerischer impedance was added into the parallel circuit [6], did not give satisfactory fitting results and the error in Gerischer impedance resistance was very high and therefore these data will not be discussed in more detail in this paper. Thus, the surface exchange process seems not to be a rate-determining step for the 70%LSCO + 30%CGO|CDO interface. According to the results of fitting, the arc 2 at low temperature and negative potentials characterises the kinetically mixed, charge transfer (with corresponding resistance R_2, Fig. 8a) and diffusion-like limited oxygen reduction processes ($\delta \leq -25°$ at $\Delta E = 0$). According to the fitting data, the diffusion resistance R_D (Fig. 8b) and R_2

(Fig. 8a) decrease nearly exponentially with rising the negative potential, which can be explained by the charge transfer process with the Arrhenius-like activation mechanism [13, 14, 18, 20]. The dependence of R_D on ΔE, indicates the very complicated mass transfer process as the resistance of the semi-infinite Fick-like diffusion process has to be independent of ΔE. The surface diffusion, Knudsen-like and finite-length diffusion as well as migration of charged oxygen species are possible [46]. The low-frequency capacitance C_2 (i.e. adsorption, absorption or pseudocapacitance of the reduction process (C_2 has the values from 200 μFcm^2 to 40,000 μFcm^2) decreases with rising temperature, except at very negative ΔE and $T > 973$ K, where C_2 does not depend on ΔE. The increase of C_2 with $|\Delta E|$ at lower temperature can be explained by accumulation (adsorption or absorption) of the negatively charged oxygen anions into the porous cathode material as well as by increase of the pseudocapacitance of the oxygen reduction reaction at moderate temperature and ΔE.

The values of $\alpha_W \leq 0.5$ (Fig. 8c) indicate that there are deviations from the classical semi-infinitive diffusion model toward the generalised finite length Warburg diffusion model i.e. toward the anomalous diffusion model with the adsorption boundary condition [43–45]. The dependence of the so-called frequency factor T_W ($T_W = L^2 D^{-1}$) on ΔE and T (Fig. 8d) indicates the quicker reduction of the reaction layer thickness with the rise of negative polarisation at lower T than at higher temperature. At fixed T, the values of T_W decrease noticeably with the rise of $|\Delta E|$.

The medium frequency charge transfer resistance R_1 decreases with increasing temperature as well as $|\Delta E|$. The medium-frequency CPE constant A_1 is maximal at lower temperature (Fig. 8e) and at moderate negative electrode potentials ($\Delta E \approx -0.2...0.3$ V). Constant A_1 decreases with rising temperature.

Activation energy and Tafel-like overpotential versus current density plots

The capacitive parts of the impedance spectra (Z'', Z'-plots at $f < 10$ kHz) were used to determine the total polarisation resistance of oxygen reduction (R_p) from the difference between the intercepts of the very low and high frequency parts of the spectra with the Z'-axis of Nyquist plots. R_p allows the quantification of the total potential loss of the overall cathodic (reduction) processes, taking into account the ohmic and activation polarisations, as well as the mass transport limitation characteristics for oxygen reduction process. Including the medium frequency arc 1 and low-frequency arc 2, the cathode polarisation resistance R_p is less than 2 Ωcm^2 at $T = 973$ K, and about 90 Ωcm^2 at $T = 773$ K. Somewhat smaller R_p values have been obtained for pure LSCO|CGO half-cell at the same temperatures [35–37]. On the other hand, the fitting data can be used for obtaining the polarisation resistance values for the medium-frequency process (arc 1), R_{p1}, and low-fre-
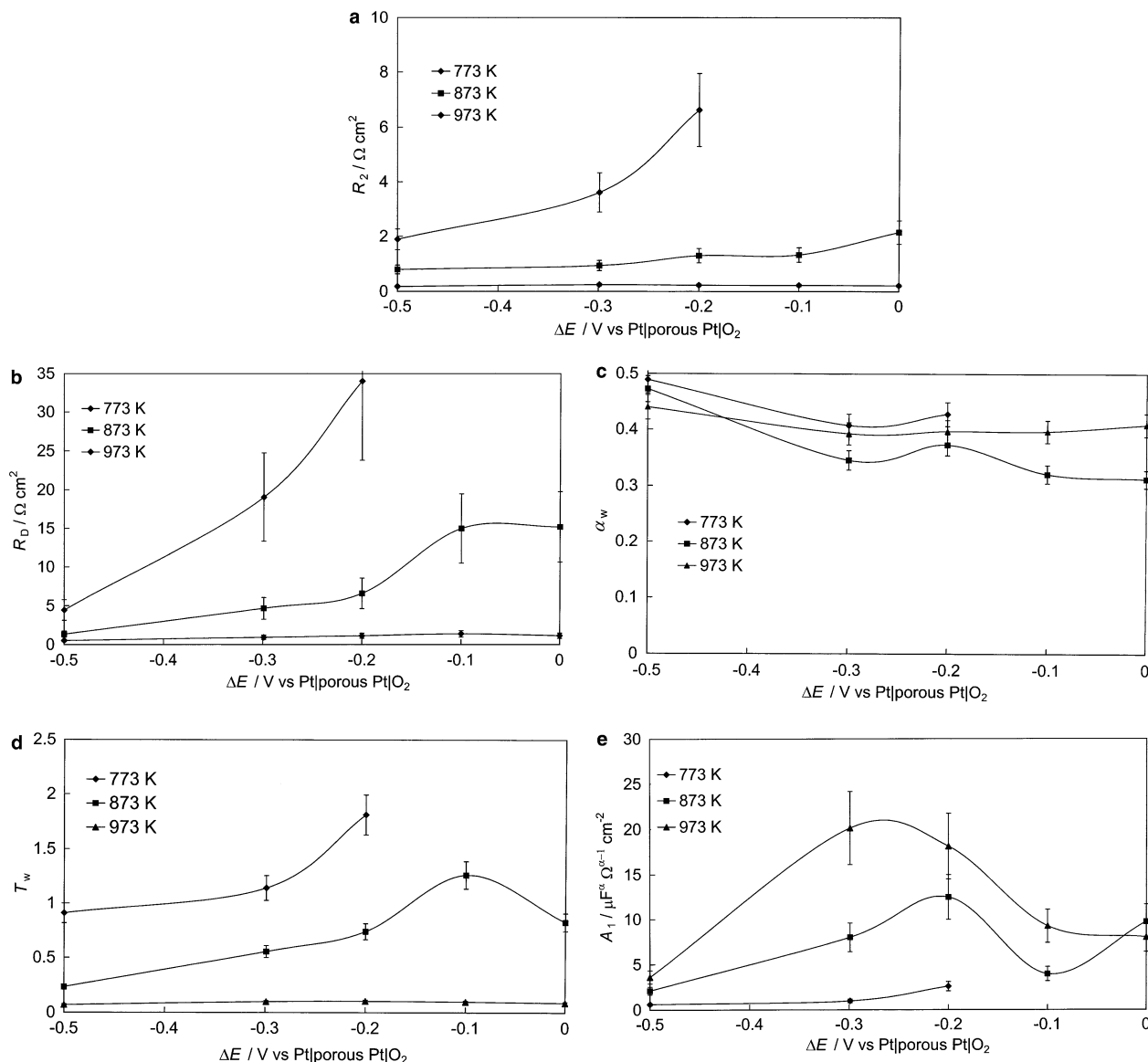
Fig. 8 Low-frequency charge transfer resistance R_2 (**a**), diffusion resistance R_D (**b**), fractional exponent α_W (**c**) and so-called frequency factor T_W (**d**) of the generalised finite-length diffusion impedance, and medium frequency constant A_1 (**e**) versus electrode polarisation dependences for the 70 wt% $La_{0.6}Sr_{0.4}CoO_{3\delta}$ + 30 wt% $Ce_{0.8}Gd_{0.2}O_{1.9}|Ce_{0.8}Gd_{0.2}O_{1.9}$ half-cell, obtained using the fitting circuit b in Fig. 7a

quency process, R_{p2}, at fixed ΔE. The R_p, R_{p1} and R_{p2} have been used for the calculation of the cathode reaction conductivity σ_t, σ_1 and σ_2 values. The linear dependences of $\log\sigma_t$ on $(T)^{-1}$ (the so-called Arrhenius plots) as well as the Arrhenius plots for arc 1 (σ_1) and arc 2 (σ_2) at fixed ΔE have been used for the calculation of the values of activation energy (Fig.9). At $\Delta E = 0$ V, $A_t = 1.5$; $A_1 = 1.3$; and $A_2 = 1.8$ eV (where A_t, A_1 and A_2 are the activation energies of the total polarisation and high-frequency and low-frequency processes, respectively), decreasing with the increase of the negative polarisation of LSCO + CGO.

The dependences of cathodic current density (j) on time (t) (chronoamperometry data, Fig. 10), when the cathode (working) electrode was stepped to the potentials $\Delta E = -0.05$, $-0,1$, -0.2, -0.3, -0.5, and -1.0 V (with respect to a Pt|porous Pt|O_2 reference electrode), indicate that the shape of the j, t-curves depends on T and ΔE. j increases with time at very short times ($t < 5$ s) but j is practically independent of time at $t \geq 5$ s. The increase in j with short times can be explained by the not very low series resistance values for the composite cathode material, by the measurable reduction overpotential of the system, as well as by slow diffusion of the partially reduced oxygen species. At higher temperatures the stable current density values have been established at more short times. Thus, at lower T and ΔE, the oxygen reduction is probably limited by the mass transfer step of the oxygen species to the reaction zone and the 70% LSCO + 30% CGO|CGO gas interface reaction does not contribute significantly to the overall reaction. At
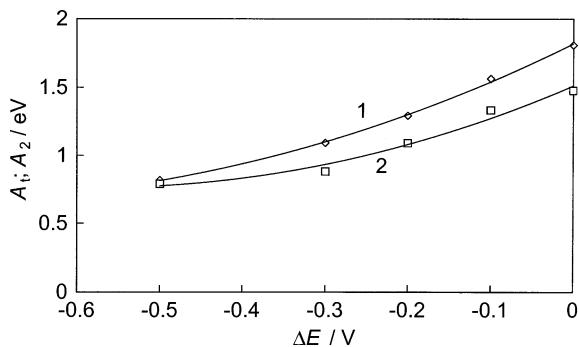
Fig. 9 Activation energy of the low-frequency process (1) and total activation energy (2) versus electrode polarisation plots for the 70 wt% $La_{0.6}Sr_{0.4}CoO_{3\ \delta}$ + 30 wt% $Ce_{0.8}Gd_{0.2}O_{1.9}|Ce_{0.8}Gd_{0.2}O_{1.9}$ half-cell, obtained from the fitting data according to the circuit b (Fig. 7a)

Fig. 11 Overpotential versus current density plots for the 70 wt% $La_{0.6}Sr_{0.4}CoO_{3\ \delta}$ + 30 wt% $Ce_{0.8}Gd_{0.2}O_{1.9}|Ce_{0.8}Gd_{0.2}O_{1.9}$ half-cell at temperatures, noted in figure

higher temperatures and higher negative potentials, the reaction is probably less controlled by the rate of transfer of the partially reduced oxygen species. The increase in concentration of the oxygen vacancies will improve the diffusion of the "charged species", leading to the increase of catalytic activity. These results are in agreement with the values of the transfer coefficient, obtained from the Tafel-like η, log j-curves (presented in Fig. 11, calculated from the j, t-curves at $t > 10$ s, where the stable values of j have been established at fixed ΔE (the values of ΔE have been corrected by the ohmic potential drop) to obtain the values of overpotential η). According to these calculations, α_c nearly equal to 1.0 has been established at lower temperature. Thus, the O_{ads} diffusion-like step seems to be the rate determining step for the electroreduction reaction [17, 46–48] in agreement with the impedance spectroscopy data. The values of the exchange current density j_0 [47], obtained at fixed temperatures, increase with T and there is nearly linear dependence of $\ln j_0$ on T (Fig. 12), indicating the Arrhenius-like activation process (except at very high temperatures where the j_0, T-plot deviates from linearity).

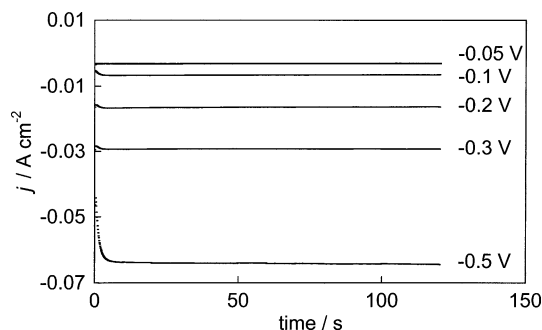The long-term stability has been tested at $T = 973$ K and $\Delta E = -0.3$ V during 3000 hours for the 70%LSCO

+ 30%CGO|CGO system. It should be noted that during the operation period at least 35 thermocycles have been made. The ac impedance measurements (Fig. 13) distinguished the electrolyte and cathode reaction resistance values practically independent of operation time of the half-cell and thermocycle number. The results of fitting the Nyquist plots show that there are no big changes during 1000 hours in the equivalent circuit parameters and only a small decrease in R_D, R_2 and C_2 values, as well as R_1 and C_1 values has been established. However, the small increase of R_{gb} has been found after $t > 1000$ hours, indicating that the weak degradation of grain boundary is possible. According to the experimental results obtained, the 70 wt% LSCO + 30 wt% CGO|CGO half-cells can be used for the future operation-time tests going on in our laboratory.

Conclusions

The kinetically mixed process (slow mass transport and electron transfer stages) takes place at the $Ce_{0.8}Gd_{0.2}O_{1.9}|70$ wt% $La_{0.6}Sr_{0.4}CoO_{3-\delta}$ + 30 wt % $Ce_{0.8}Gd_{0.2}O_{1.9}$ semi-cell in air at $773 \leq T \leq 1,073$ K. The values of activation energy, decreasing with the increasingly negative polarisation, and of the charge transfer coefficient $\alpha_c \approx 1.0$ at $T \leq 773$ K indicate that the mass transfer

Fig. 10 Chronoamperometry data for the 70 wt% $La_{0.6}Sr_{0.4}CoO_{3\ \delta}$ + 30 wt% $Ce_{0.8}Gd_{0.2}O_{1.9}|Ce_{0.8}Gd_{0.2}O_{1.9}$ half-cell at temperature 873 K and electrode polarisations (V), noted in figure
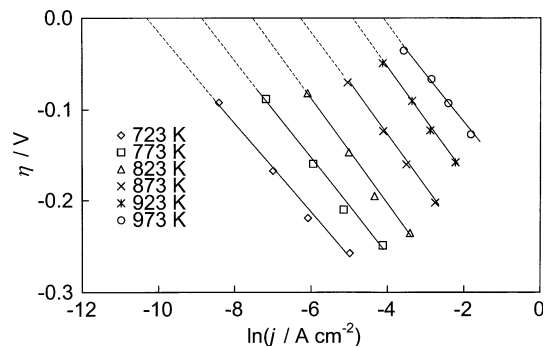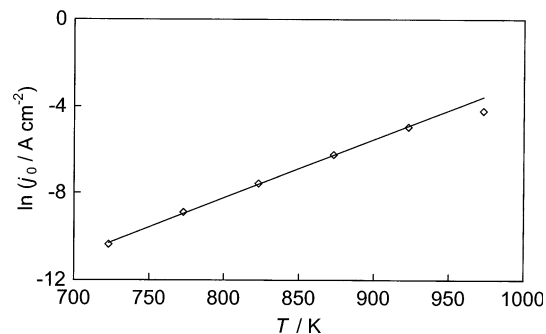

Fig. 12 Exchange current density versus temperature dependences, obtained from Fig. 11
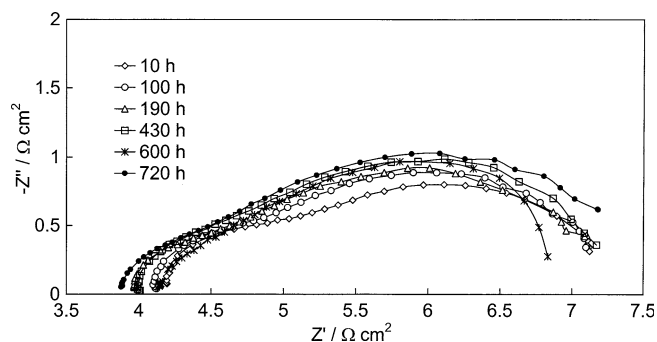
Fig. 13 Nyquist plots for Sys 1 at $\Delta E = -0.2$ V at temperature 873 K at different operation times, shown in figure

limited process of the negatively charged oxygen species inside porous solid cathode material is the rate-determining step in agreement with the fitting results of the Nyquist plots. The values of diffusion resistance and charge transfer resistance for the 70 wt% LSCO + 30 wt% CGO|CGO interface decrease with the rise of temperature and cathodic polarisation. The noticeable dependence of the diffusion resistance as well as phase angle on cathodic polarisation at fixed temperature indicates the complicated mass transfer process mechanism of the oxygen species.

References

1. Takeda Y, Kanno R, Noda M, Tomida Y, Yamamoto O (1987) J Electrochem Soc 134:2656
2. Mizusaki J, Mima Y, Yamauchi S, Fueki K, Tagawa H (1989) J Solid State Chem 80:102
3. Minh NQ (1993) J Am Ceram Soc 76:563
4. van Hassel BA, Kawada T, Sakai N, Yokokawa H, Dokiya M, Bouwmeester HJM (1993) Solid State Ionics 66:295
5. Reinhart G, Baitinger V, Göppel W (1995) Ionics 1:504
6. Adler SB, Lane JA, Steele BCH (1996) J Electrochem Soc 143:3554
7. Mizusaki J, Tabaci J, Matsuura T, Yamauchi S, Fueki K (1989) J Electrochem Soc 136:2082
8. Kilner JA, De Souza RA, Fullarton IC (1996) Solid State Ionics 86–88:703
9. Hibbert DB, Tseung ACC (1978) J Electrochem Soc 125:74
10. Carter S, Selcuk A, Chater RJ, Kajda J, Kilner JA, Steele BCH (1992) Solid State Ionics 53–56:597
11. Steele BCH (1995) Solid State Ionics 75:157
12. Philips MB, Sammes NM, Yamamoto O (1999) Solid State Ionics 123:131
13. Gödickemeier M, Sasaki K, Gauckler LJ, Riess I (1996) Solid State Ionics 86–88:691
14. Mogensen M, Sammes NM, Tompsett GA (2000) Solid State Ionics 129:63
15. Adler SB (1998) Solid State Ionics 111:125
16. Siebert E, Hammouche A, Kleitz M (1995) Electrochim Acta 40:1741
17. Wang S, Lu X, Liu M (2002) J Solid State Electrochem 6:384
18. Jiang SP (2002) Solid State Ionics 146:1
19. Tu HY, Takeda Y, Imanishi N, Yamamoto O (1999) Solid State Ionics 117:277
20. Dusastre V, Kilner JA (1999) Solid State Ionics 126:163
21. ten Elshof JE, Bouwmeester HJM, Verweij H (1996) Solid State Ionics 89:97
22. Steele BCH (2000) Solid State Ionics 129:95
23. Tai L-W, Nashrallah MM, Anderson HU, Sparlin DM, Sehlin S R (1995) Solid State Ionics 76:259
24. Sahibzada M, Steele BCH, Barth D, Rudkin RA, Metcalfe IS (1999) Fuel 78:639
25. Wang S, Kato T, Nagata S, Honda T, Kaneko T, Iwashita N, Dokiya M (2002) Solid State Ionics 146:203
26. Wang S, Kato T, Nagata S, Honda T, Kaneko T, Iwashita N, Dokiya M (2002) J Electrochem Soc 149:A927
27. Kharton VV, Kovalevsky AV, Viskup AP, Shaula AL, Figueiredo FM, Naumovich EN, Marques FMB (2003) Solid State Ionics 160:247
28. Weber A, Ivers-Tiffee E (2004) Power sources. http://www.sciencedirect.com, online
29. Inaba H, Tagawa H (1996) Solid State Ionics 83:1
30. Kharton VV, Yaremchenko AA, Naumovich EN (1999) J Solid State Electrochem 3:303
31. Manning PS, Sirman JD, Kilner JA (1997) Solid State Ionics 93:125
32. Lane J A, Kilner J A (2000) Solid State Ionics 136–137:927
33. Ji Y, Kilner JA, Carolan MF (2004) J Eur Ceramic Soc 24:3613
34. Nurk G, Kallip S, Kivi I, Möller P, Lust E (2004) Ext. abstracts of 6th European solid oxide fuel cell forum, Lutzern, p 887
35. Lust E, Nurk G, Moller P, Kivi I, Kallip S, Janes A, Mändar H (2003) In: Proceedings of the international symposium on solid oxide fuel cells. Paris, p 1176
36. Nurk G, Möller P, Kivi I, Kallip S, Jänes A, Lust E (2003) Medium temperature half-cells for SOFCs. Extend Abstr of SOFC Forum. Miami Beach, p 427
37. Lust E, Nurk G, Kallip S, Kivi I, Möller P, Nigu P (2005) Electrochemical and impedance characteristics of some medium temperature half-cells for SOFC. J Electrochem Soc (in press)
38. MacDonald RJ, ZView for Windows (Version 2.7). Scribner, Southern Pines
39. Macdonald JR, Johnson WB (1987) In: Maclonald JR (ed) Impedance spectroscopy: emphasizing solid materials and systems. Wiley, New York
40. Sluyters-Rehbach M, Sluyters J (1970) In: Bard A (ed) Electroanalytica chemistry, vol 4. Macel Dekker, New York, p 76
41. Lasia A (1999) In: Conway BE, Bockris J O'M, White RE (eds) Modern aspects of electrochemistry, vol 32. Kluwer/Plenum, New York, p 143
42. Gabrielli C (1995) In: Rubinstein I (ed) Physical electrochemistry—principles, methods and application. Marcel Dekker, New York, p 257
43. Jacobsen T, West K (1992) Electrochim Acta 40:233
44. Bisquert J, Garcia-Belmonte G, Fabregat-Santiago F, Bueno RR (1999) J Electroanal Chem 475:152
45. Bisquert J, Compte A (2001) J Electroanal Chem 499:112
46. Chan SH, Chen XJ, Khor KA (2004) J Electrochem Soc 151:A164
47. Kim JW, Virkar AV, Fung KZ, Metha K, Singhal SC (1999) J Electrochem Soc 146:69
48. van Heuveln FH, Bouwmeester HJM (1997) J Electrochem Soc 144:134